



AIAA-2001-0126
FLAPPING-WING PROPULSION
FOR A MICRO AIR VEHICLE

K.D.Jones, S.J.Duggan and M.F.Platzer
Naval Postgraduate School
Monterey, CA

39th Aerospace Sciences
Meeting & Exhibit
8-11 January 2001 / Reno, NV

FLAPPING-WING PROPULSION FOR A MICRO AIR VEHICLE

K. D. Jones,[†] S. J. Duggan[‡] and M. F. Platzer*

Naval Postgraduate School
Monterey, California

Abstract

Recent interest in the development of micro air vehicles has led to a renewed interest in flapping-wing propulsion due to the spectacular performance of small birds and insects in this flight regime. Small flapping-wing models, no bigger than 15 centimeters in any dimension, are designed, built and tested in a low speed wind-tunnel. The composite models weigh as little as 6 grams, and flap at frequencies in excess of 38Hz. Both qualitative and quantitative data are obtained. A smoke-wire is used to visualize the highly unsteady, three-dimensional flowfields, providing some insight into the complicated nature of the flow, with comparisons to numerical models where possible. Operating in the Reynolds number range below 24,000, flow visualization indicates separated flow over most of the flapping cycle. Direct thrust measurements are made for several configurations, and illustrate the advantages of aeroelastic tailoring of the structure. While many of the model's aerodynamic characteristics still need further investigation, the present model produces sufficient thrust to hover, and it overcomes its own drag at speeds up to 5.5 meters per second.

Nomenclature

AR = aspect ratio, b/c
 b = wing span
 c = chord length
 C_d = drag coefficient, $D/(q_\infty S)$
 C_l = lift coefficient, $L/(q_\infty S)$
 C_m = moment coefficient, $M/(q_\infty cS)$
 C_p = power coefficient, $-C_l \dot{y} - C_m \dot{\alpha}$
 C_t = thrust coefficient, $T/(q_\infty S)$
 D = drag
 f = frequency in Hertz
 h = plunge amplitude in terms of c
 h_{te} = plunge amp. of the trailing edge in terms of c
 k = reduced frequency, $2\pi fc/U_\infty$
 L = lift

M = moment
 q_∞ = freestream dynamic pressure, $\rho_\infty U_\infty^2/2$
 R_L = chord Reynolds number, $U_\infty c/\nu_\infty$
 S = wing area
 St = Strouhal number, $2fh_{te}/U_\infty = kh_{te}/\pi$
 t = time
 T = thrust ($-D$)
 U_∞ = freestream velocity
 x_p = pivot location from LE in terms of c
 $y(\tau)$ = vertical displacement in terms of c
 α = angle of attack
 $\Delta\alpha$ = pitch amplitude in degrees
 ϕ = phase between pitch and plunge
 η = propulsive efficiency, C_t/C_p
 ν_∞ = freestream kinematic viscosity
 ρ_∞ = freestream density
 τ = nondimensional time, tU_∞/c
 $(\dot{})$ = rate of change w.r.t. τ

Introduction

The use of flapping-wing propulsion dates back much further than the forms of propulsion considered to be *conventional* in today's mechanical world. Indeed, nature has predominantly selected flapping-wing propulsion as the optimal approach, however, whether this choice is one of organic constraints or one of optimal performance is an unsettled matter. Nevertheless, the fact that birds, insects and many sea creatures utilize flapping-wing propulsion with great success, at the very least, merits a thorough scientific investigation. Of course, this is primarily an academic argument to pursue the topic, one which, until recently, has chiefly relegated flapping-wing research to something of a hobby-like status. The necessary financial support for more dedicated research has recently come about as a result of DARPA's interest in the development of Micro Air Vehicles (MAVs).

The scientific history of flapping-wing propulsion is rather lengthy, dating back nearly a century to the related but independent papers of Knoller¹ and Betz,² in 1909 and 1912, respectively. For a historical summary of flapping-wing propulsion research and developments, please refer to Jones *et al.*³ For continuity, several past investigations by the present authors and colleagues are briefly described here.

[†]Research Assistant Professor, Senior Member, AIAA

[‡]Graduate Student, Captain, Canadian Armed Forces

*Professor, Fellow, AIAA

This paper is declared a work of the U.S. Government and is not subject to copyright protection in the United States.

In 1998, Jones *et al.*⁴ compared wake structures behind flapping wings experimentally photographed in a water tunnel and numerically predicted using an unsteady panel method that employed a deforming wake model. They demonstrated that the formation and evolution of the unsteady wakes was essentially an inviscid process over a broad range of Strouhal numbers. Additionally, an unusual phenomenon was discovered for highly energetic flapping, where a symmetric airfoil undergoing symmetric motion produced an asymmetric or deflected wake, yielding both an average thrust and lift. This phenomenon was duplicated both numerically and experimentally as shown in Fig. 1, with a schematic depicting the location and orientation of the primary eddies shown at the top, the numerically predicted wake topology shown in the middle, and the experimentally photographed wake topology shown at the bottom. While this phenomenon was of little practical use (the predicted propulsive efficiencies at these extreme conditions were quite low) it illustrated the success of relatively primitive numerical methods in capturing highly non-linear or chaotic flow physics. Note the maximum induced angle of attack for the simulation shown in Fig. 1 exceeded 56 degrees, well beyond the airfoil's stall boundary.

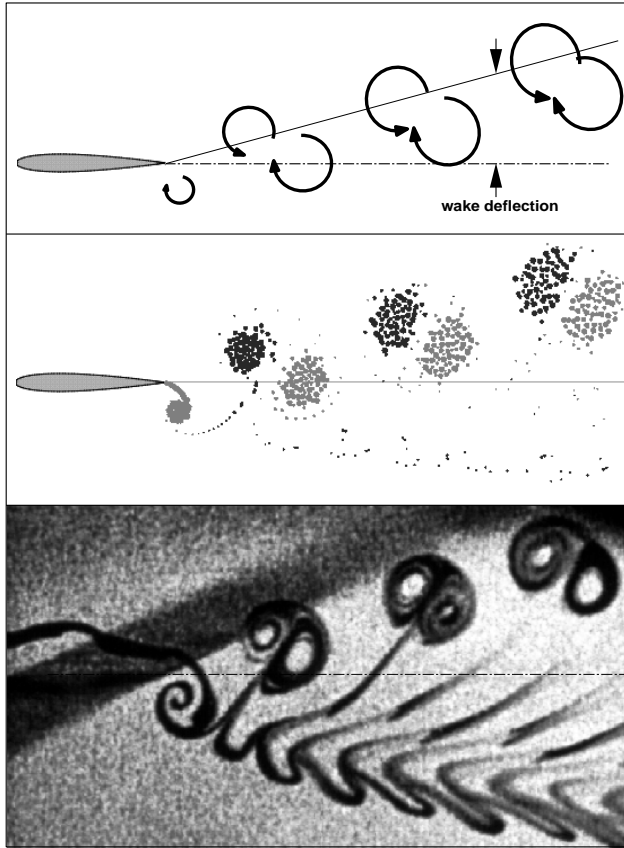


Fig. 1: Deflected wake comparison ($kh=1.5$).

The Strouhal number is usually considered to be the definitive non-dimensional parameter in wake dominated flows such as these, but Jones and Platzer⁵ showed that the Strouhal number is sometimes a poor indicator of flapping-wing performance, as shown in Figs. 2 and 3, where the Strouhal number was fixed at a relatively low value, 0.03 ($hk = 0.1$), and the ratio of h and k was varied. Clearly the wake instability increased with k , which corresponded to a reduction in performance. The panel code was compared with the predictions of Garrick's linear theory⁶ and an unsteady, two-dimensional Euler solver. The wake images are scaled such that the wake wavelengths are the same.

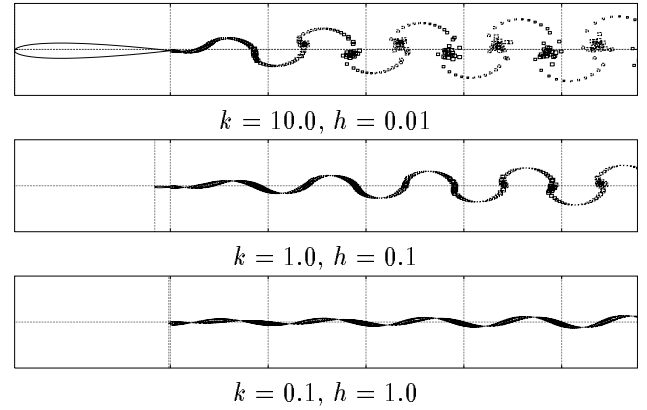


Fig. 2: Dependence of wake instability on k .

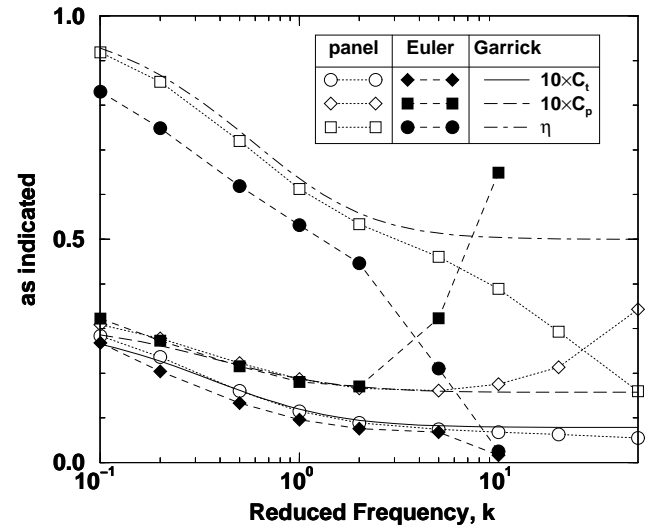


Fig. 3: Thrust performance for constant $St/0 > 1$.

A number of flapping-wing configurations were evaluated by Jones and Platzer,^{5,7,8} shown in Fig. 4. Configuration (a) is the single airfoil case. Configuration (b) simulates the Schmidt *wave-propeller*,⁹ where the forward wing flaps, and the trailing airfoil is stationary, recuperating some of the vortical energy ex-

pendent by the forward wing in the form of additional thrust. Configuration (c) is the *opposed-plunge* case, or the numerical model of flapping near a ground plane. Configuration (d) simulates Schmidt's wave-propeller near a ground plane, and configuration (e) is a mechanically simpler form of configuration (c) which is presently used for the MAV models.

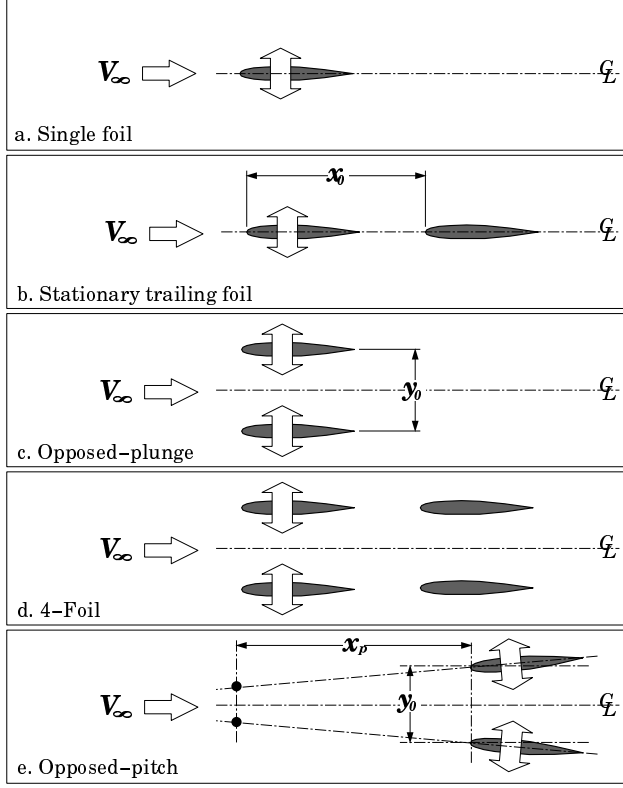


Fig. 4: Numerical and experimental configurations.

Jones and Platzer⁵ showed a marked performance improvement for the opposed-plunge case (c), as shown in Figs. 5 and 6, where configurations (a), (b) and (c) were evaluated using the unsteady panel code. The conditions for this experiment were set by the limitations of an experimental flapping-wing mechanism, with $h = 0.4$, $x_0 = 2.2$ for (b) and $y_0 = 1.4$ for (c). The airfoil used was a NACA 0014. For (a) the panel code actually predicted a greater thrust than linear theory, but at a lower efficiency. For (b) and (c) the average thrust and efficiency for the two wings is shown. The forward wing generated almost all of the thrust in (b), but both airfoils contributed equally in (c). Note that the opposed-plunge case (c) yields a considerable increase in thrust over (a) and nearly double the thrust of (b). While Schmidt's wave-propeller (b) should have the highest efficiency, note that this was an inviscid analysis, and viscous losses would diminish the efficiency of (b) much more than (c) due to the lower thrust coefficient of (b).

From a practical point of view, an additional advantage of configuration (c) is that it offers a mechanically and aerodynamically balanced system. This makes experimental testing much easier and provides a more useful platform for many sensor payloads where fluctuating heading and vibration could be problematic. Note, the opposed plunge case emulates a single flapping wing near a ground plane. Watching birds fly low over water, it is clear that they have discovered this performance enhancement. Of course, the advantage of having two opposed wings is that the vehicle can gain the benefits of ground effect without having to be near the ground.

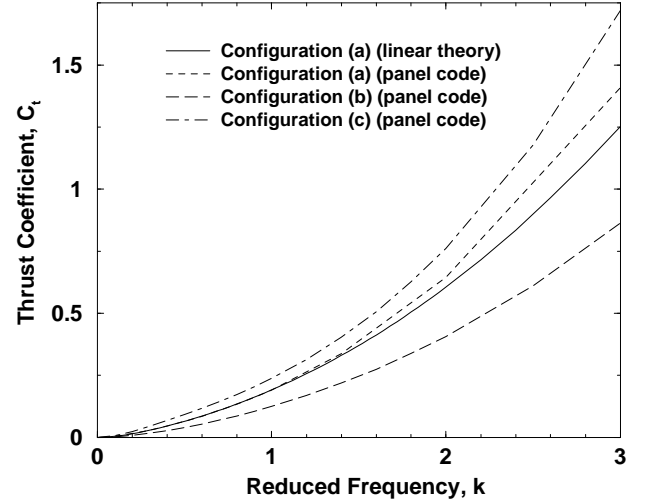


Fig. 5: Thrust coefficient versus reduced frequency.

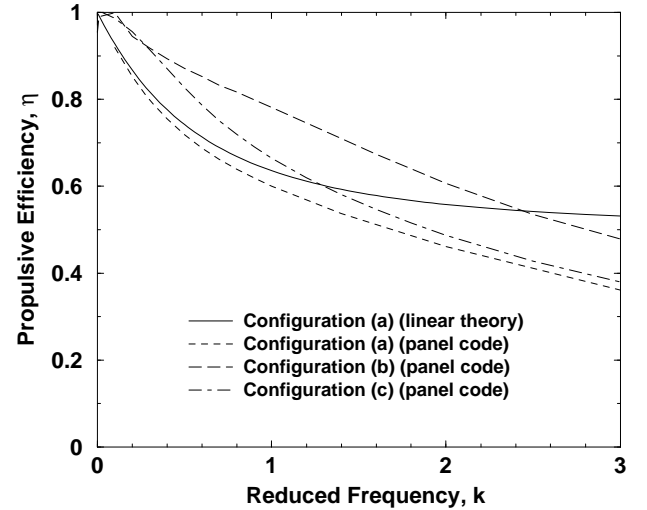


Fig. 6: Efficiency versus reduced frequency.

In order to evaluate the application of the panel code as a flapping-wing design tool, an experimental model capable of performing pitch/plunge oscillations of two wings with variable geometry was de-

signed, as shown in Fig. 7. The model and the measured performance were detailed by Jones and Platzer⁷ and Lund.¹⁰ The model flapped two airfoils resembling NACA 0014s, with a chord length of 64mm and an effective span of 1200mm, with variable pitch and plunge amplitudes. The model was suspended by four cables from the tunnel ceiling, such that it could swing freely in the streamwise direction, as shown in Fig. 8. Thrust was determined by measuring the streamwise deflection of the model when the wings were flapped. The deflection was measured by bouncing a laser sensor off a small notch on the back of the rear nacelle, as shown in Fig. 7.

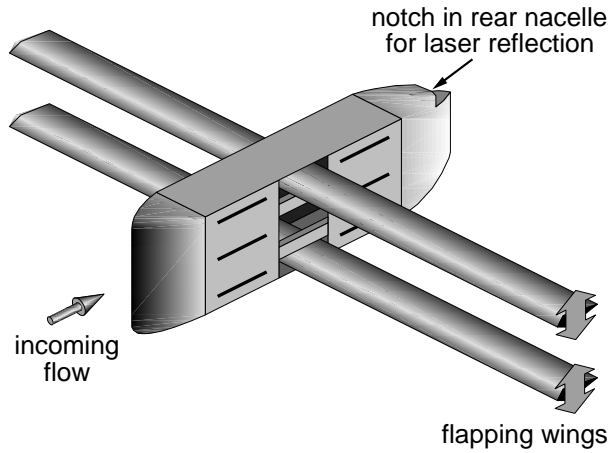


Fig. 7: Isometric view of the large model.

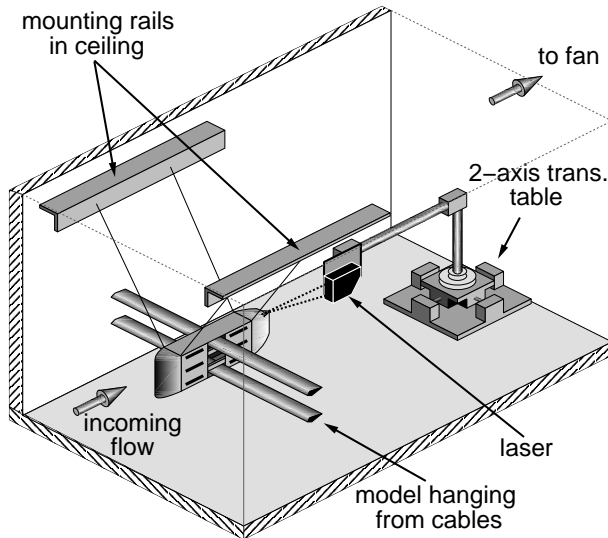


Fig. 8: View of the large model in the test-section.

Results from Jones and Platzer⁷ with velocities corrected by Lund¹⁰ and improved numerical results are shown in Fig. 9 for (c) with $h = 0.4$ and $y_0 = 1.4$. Reynolds numbers for the experiment varied between 0 and about 45,000. Of particular interest, note the dip in thrust for the 8 Hz case when the velocity

dropped below 5m/s. This *drag-bucket* was thought to be caused by flow separation over part or all of the cycle, as the induced angle of attack exceeded 14 degrees for velocities below 5m/s.

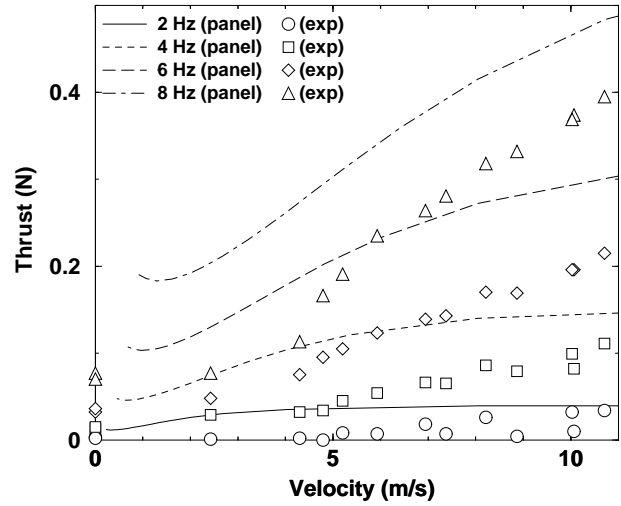


Fig. 9: Thrust for pure-plunge motion of (c).

With the reasonable success at predicting propulsive performance on the large model, Jones and Platzer⁸ and Duggan¹¹ designed, built and tested much smaller, MAV-sized models, nominally with a 15cm span and length. For mechanical simplicity, a slight variation of the flapping motion was adopted for the MAV models, depicted as configuration (e) in Fig. 4. Instead of a pure-plunge motion, a pure-pitch motion was used, with the pitch axis located several chord lengths in front of the wing. A cross-sectional drawing of a typical MAV is shown in Fig. 10, where the flow goes from left to right. An isometric view of the model is shown in Fig. 11.

The models utilized exceptionally small, geared, stepping motors from RMB Smoovy. The motors were 5mm in diameter and, with a 25:1 planetary gear system, they were about 25mm long and weighed a meager 2.4g. Nominally, they produced a torque of about 2.5mNm at speeds up to about 800 RPM (the rated limit of the gearbox), which yielded a maximum power of roughly 0.21 watts. The brushless motors were controlled by an oscillatory, open-loop driver circuit, which allowed for very precise, steady and reproducible rotational speeds. While the motor had a reported max speed of around 100,000 RPM, the gearbox was only rated for 20,000 RPM input, which limited the flapping frequency to around 13 Hz, however, with some models, sustained frequencies of over 18 Hz were reached. Presently, a closed-loop controller is used, providing 2 to 3 times the power. This will be discussed in greater detail in the next section. The flap-

ping motion was generated via a small spring-steel crankshaft coupled to the gearbox with thin-wall silicon tubing. The crankshaft moved the flapping-beams via Scotch yokes constructed of very thin piano wire.

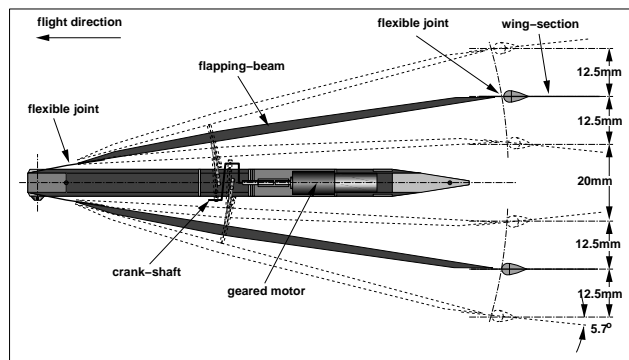


Fig. 10: Schematic of a 15cm MAV model.

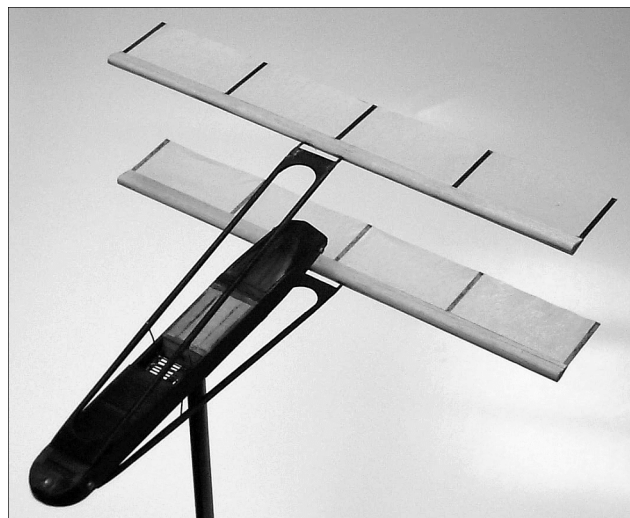


Fig. 11: Isometric view of a 15cm MAV model.

Static testing (wind-off) was performed to evaluate the sensitivity to airfoil shape and aspect-ratio. The best wing design tested utilized a small tear-drop shaped balsa leading edge, roughly $6\text{mm} \times 4\text{mm}$ in section, with thin carbon-fiber strips for ribs and Japanese tissue for the primary wing surface. It was also found that, at least for the wind-off case, the aspect ratio did not play an important role for values above about 4. Typical thrust measurements are shown in Fig. 12, for the model using wings with a 36mm chord and elastic wing mounts. The elastic wing mounts allowed the angle-of-attack to fluctuate aeroelastically, reducing the instantaneous effective angle of attack, and almost always increasing the performance.

Surprisingly, the maximum thrust always occurred at zero flight-speed, opposite to the predictions of the panel code, and where the induced angle of attack was roughly 90 degrees (minus the aeroelastic incidence).

At quite low flight speeds the thrust was found to drop quickly and then recover slightly at higher speeds. Interestingly, the minimum thrust was always found with a Strouhal number of about 0.23, nearly the natural shedding frequency of a cylinder at comparable Reynolds numbers.

It was conjectured that the MAVs operated with fully separated flow over the full flight regime, and that apparently the separation benefited the performance at very low flight speeds, and detracted from the performance at higher speeds. However, without any flow visualization, the loss in performance could not be fully understood.

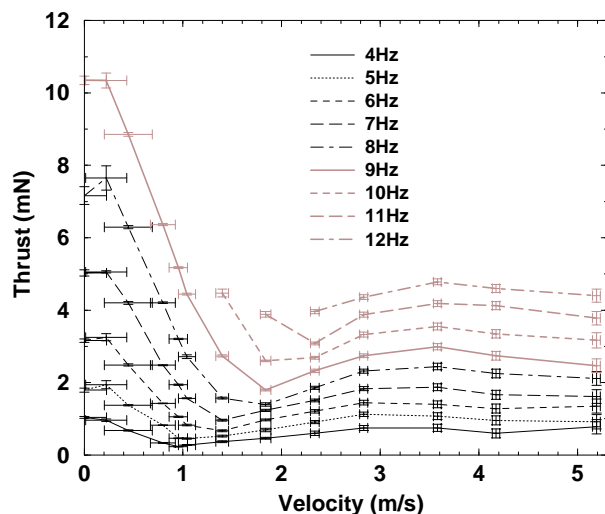


Fig. 12: Typical MAV thrust measurements.

The present study is a continuation of the development and testing of flapping-wing MAVs, using improved measurement techniques and newer designs and construction materials. Additionally, a method for flow visualization in the low-speed range has been developed.

Approach

In this section, the numerical methods utilized are briefly summarized, with references for a more complete description. The present design and construction is described and the experimental methods employed to measure the vehicle performance are described in detail.

Numerical Methods

Flow solutions are computed using an unsteady, two-dimensional, potential-flow code originally developed by Teng,¹² and extended to multiple airfoil solutions by Pang.¹³ The airfoil paneling follows the approach of Hess and Smith¹⁴ with the unsteady wake modeling following the approach of Basu and Hancock.¹⁵

The unsteady panel code has been extensively documented. See Jones and Platzer⁸ for a more elaborate description and a list of references further documenting the panel code.

Nomenclature

The general equations of motion for the flapping wings are given in Fig. 13. All equations are non-dimensional, using the airfoil chord as the reference length and the freestream velocity as the reference speed.

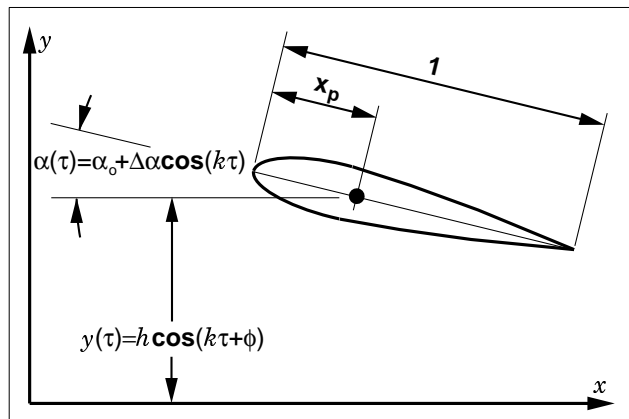


Fig. 13: Equations of motion & nomenclature.

Experimental Methods

The MAV model used in the present study is a variation of the model used in the previous study. Earlier models were built with weights below 6 grams, however, for wind-tunnel testing this offered no advantage. The models actually need to be weighted down significantly. Consequently, the present model has a dry weight of about 9 grams, and with all the spare volume in the fuselage filled with lead, it weighs about 25 grams. For the most energetic tests, additional external ballast is added giving the model a weight of over 38 grams. This ballast is a requirement of the present thrust measurement technique, which will be described later. The newer model provides a greater degree of modularity, allowing for motor, gearbox and crankshaft substitutions as well as sting-mounting and interchangeable rear nacelles. Additionally, the 3-pole, brushless stepping-motor is now mounted in a brass heat-sink, as the open-loop controller causes the motors to run very hot (≈ 100 degrees C).

As before, the model is primarily built out of balsa wood and epoxy-graphite laminates, but the Japanese tissue used for the wing surface on the old model is replaced with extremely light ($2.5g/m^2$) and transparent micro-film. The micro-film is much less durable, but its reduced weight helps achieve higher flapping

frequencies and its transparency aids in flow visualization. An isometric view of the newer model mounted on a vertical sting is shown in Fig. 14. Note the extension from the rear nacelle, supporting a small reflective surface for the laser range finder, described later. Also note the thin carbon-fiber strips attaching the wings to the flapping beams. These strips provide the aeroelastic pitching, with the width and length of the strips determining the pitch amplitude. A view of the aeroelastically deformed wings is shown in Fig. 15, with the wings coming together completely, perhaps making use of the Weis-Fogh effect. The present model has a chordlength of $36mm$, a plunge amplitude of about $10.5mm$ ($h = 0.3$), and a mean separation of about $45mm$ ($1.25c$).

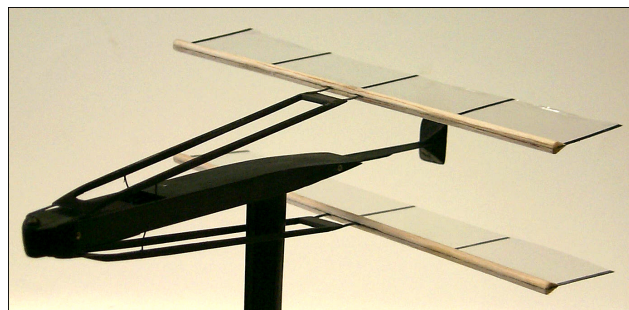


Fig. 14: Isometric view of the new MAV.

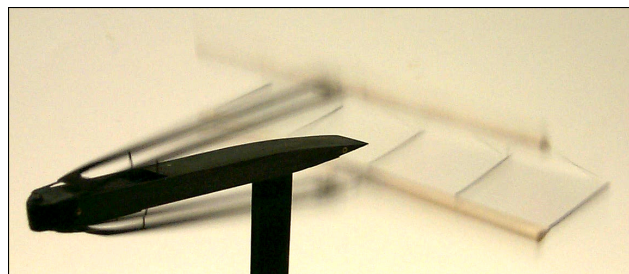


Fig. 15: Aeroelastic deflection of the wings.

The previously used open-loop controller offered the rather nice feature of maintaining a fixed motor speed indefinitely, allowing for very precise and reproducible flapping frequencies. However, since the open-loop controller received no information about the motor's speed and position, if too much torque was put on the motor, it would not advance sufficiently before the next motor pole was energized, and the motor would stall. This behavior also required the motor to accelerate slowly. Using the open-loop controller on the old MAV design, the highest flapping frequency achieved was about 18Hz, far exceeding the gear-box rating (13Hz).

In the present study a newer, closed-loop controller is used. The closed-loop controller works by picking up back-EMF from the unused motor pole to

provide rate and position data to the controller. The controller then tailors the signal to suit the motor's power requirements more efficiently. This approach requires a fourth wire to the motor, which was already available in our test apparatus (this will be described later). The motor also now runs much cooler, and can be run at exceedingly high speeds, in excess of 38Hz (motor speeds in excess of 57,000 RPM). Unfortunately, since the controller adapts the signal to suit the motor load, it no longer maintains a fixed frequency. In fact, since the motor is geared down 25:1, the rotational speed varies throughout the flapping cycle, slowing down when the aerodynamic load on the wing is high, and accelerating when the load is low. Usually the flapping frequency is reasonably stable at frequencies up to about 20Hz, but becomes unstable at higher frequencies. Additionally, the power tends to fade at the extreme speeds, as the motor and controller components heat up, and this often leads to increased experimental deviations near the peak frequencies. The precise, instantaneous motor speed is determined by measuring the voltage going to one motor pole, with 25 pulses corresponding to one flapping cycle.

The 3-pole power is fed into the model through 0.127mm diameter copper support wires, using a fourth wire for the back-EMF feedback signal. The support wires are attached to the model via small gold-plated pins, near the nose, and near the rear of the model. The mass of the wires is negligible compared to the mass of the model and the wires are flexible enough not to impede the model's motion. The model is suspended from a small splitter plate by the support wires such that it may swing freely in the streamwise direction, but remains relatively steady in all other directions, as shown in Fig. 16.

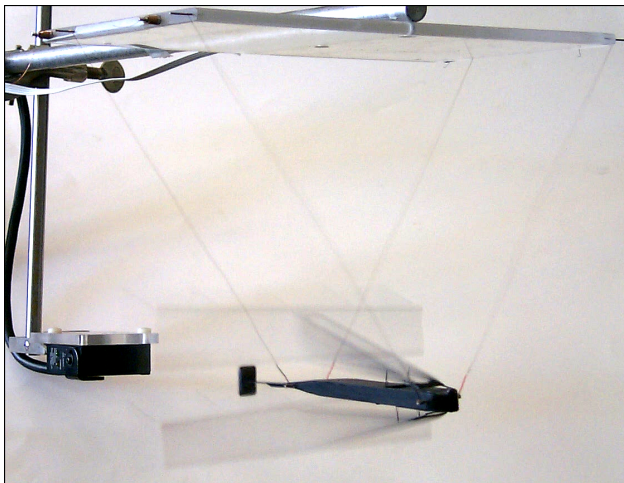


Fig. 16: Thrust measurement setup.

As the model flaps and creates thrust, it is displaced in the streamwise direction, and the displacement is measured by bouncing a laser sensor off the small reflective surface on the rear nacelle, as shown in Fig. 16. The laser analog sensor, an NAIS model ANL1651, is nominally 130mm downstream of the models, and measures distances accurately within the range 80 to 180mm. The sensor is generally about 3 to 4 chord lengths downstream of the model and is not thought to create a significant flow interference effect. The accuracy of the sensor is prescribed by the manufacturer as $\pm 100\mu\text{m} \pm 0.002 \times \Delta x$ for the range $130\text{mm} \pm 35\text{mm}$.

The thrust is computed by measuring the precise mass of the model, the length of the pendulum, and the horizontal displacement due to thrust, and using the equation

$$T = \frac{W \Delta x}{\sqrt{L^2 - \Delta x^2}} \quad (2)$$

where W is the MAV weight, L is the pendulum length and Δx is the horizontal deflection. The pendulum length is periodically checked by perturbing the model and letting it swing sinusoidally with small amplitude. The displacement signal from the laser sensor is recorded on a digital storage oscilloscope (DSO) for a 6.5 second period, and the DSO output is analyzed to determine the natural frequency. The length of the pendulum is then determined by

$$L = \frac{g}{(2\pi f)^2}. \quad (3)$$

The average deviation in the prediction of the natural frequency is used with Eq. 3 to determine the error in the length measurement.

The mass is measured on a Setra EL410D digital balance with a 0.001g accuracy. The model mass may vary by about 0.005g from day to day, due to humidity, dust and other environmental contamination.

The flapping frequency is adjusted using a strobe light as a reference, where the strobe is set to the desired frequency, and the motor speed is adjusted until the wing motion appears frozen in the light of the strobe. However, the true flapping frequency is determined by recording the voltage going to one motor pole on the DSO, and then analyzing the time-history of the voltage during post-processing. This provides both an accurate measure of the frequency and a measure of the fluctuation for error estimation. For low frequencies the fluctuations are usually quite low, but for very high frequencies the errors are sometimes large due to power-fade. Also, due to the power-fade issue, sometimes thrust data is recorded before the natural frequency oscillations die out, yielding additional uncertainty in the measurements.

Experiments are performed in the Naval Post-graduate School $1.5 \times 1.5m$ low-speed wind-tunnel. The tunnel is a continuous, flow-through facility with an approximate flow speed range between $0m/s$ and $9.5m/s$. The speed is set by varying the pitch of a fan which is driven by a constant speed motor. The tunnel has a square, $4.5 \times 4.5m$, bell-shaped inlet with a 9-to-1 contraction ratio to the $1.5 \times 1.5m$ test section. The turbulence level has been determined by Lund¹⁰ using LDV. For speeds above $1.5m/s$ the turbulence intensity was measured below 1.75% at the test section.

Flow speed in the tunnel is measured using a pitot-static tube attached to an MKS Baratron type 223B differential pressure transducer. The transducer provides a voltage that is linear with the differential pressure, yielding 1 volt at 1 torr. The flow-speed is then given by

$$U_{\infty} = \sqrt{\frac{2\Delta p}{\rho_{\infty}}} \quad (4)$$

The transducer has a reported accuracy of 0.5% of the full-scale reading which, due to the nature of Eq. 4, results in rather large errors in the measurement of low velocities but quite small errors in the measurement of high velocities. The pitot-static tube has been calibrated using LDV, and was shown to be sufficiently accurate. The LDV equipment is now being fitted with an encoder for performing time-accurate localized velocity measurements of the surrounding flowfield.

The pitot-static tube has errors associated with the measurement of both the static and total pressure. The pitot tube used here has an outer diameter of $8mm$, 8 static ports aligned symmetrically, $64mm$ (8 diameters) downstream of the tip base, and a stem approximately $120mm$ (15 diameters) downstream of the static ports. According to Pope¹⁶ the geometry of the probe should yield about a 0.5% over-prediction of the static pressure.

Reduced frequencies between about 0.1 to 10 are tested, as well as the limiting case of static thrust that yields a theoretical reduced frequency of infinity (based on free-stream speed). Chord-Reynolds numbers for this study vary between 0 and about 24,000.

Flow visualization is performed using a smoke wire, with $0.3mm$ diameter Ni-Chrome (NI80-CR20) wire stretched between two posts, and spring-loaded to account for the wire-elongation when it's heated. The resistive wire is heated by applying a voltage across its length, and smoke is generated by dripping Roscoe fog juice down the wire prior to heating it. To generate streaklines, thin copper wire ($0.254mm$ dia) is wrapped around the Ni-Chrome wire at intervals and soldered to keep it in place. For the smoke-wire used,

the wire/solder beads are spaced at $1cm$ intervals. The fog fluid tends to pool on the beads, and it takes some time for the wire to burn off these deposits, providing 5 to 10 seconds of continuous smoke. The undisturbed smoke rake can be seen in Fig. 17 with a wind-speed of $1.5m/s$. With slightly more detail, it can be seen that most of the streaklines are really two, closely spaced lines. Typically the fluid pools above and below the beads, and it's these two deposits that burn and create the pairs of lines.

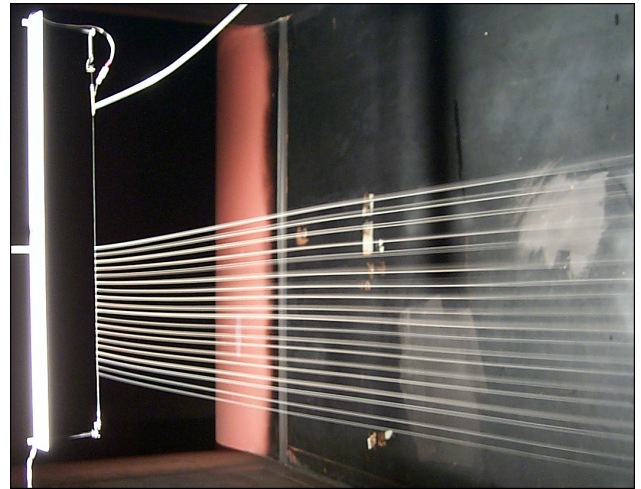


Fig. 17: The smoke-wire setup.

For a few tests the model is fitted with small tip-plates, attempting to reduce tip-losses. The tip-plates are constructed out of balsa, carbon-fiber and micro-film, and can be seen in Fig. 18.

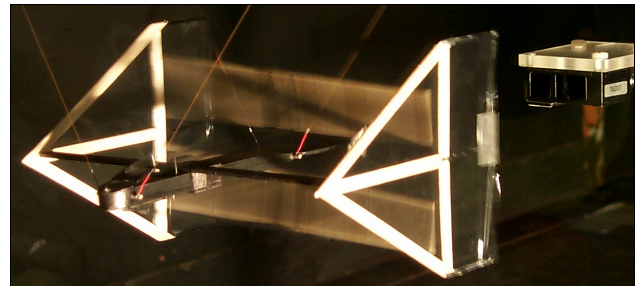


Fig. 18: The MAV fitted with tip-plates.

Results

Results are provided in the sections below for the numerical predictions of the panel code, qualitative experimental results using flow visualization with comparisons to the panel code, and quantitative measurements of thrust on the model.

Numerical Predictions

The application of panel methods for the simulation of the MAV flowfields is certainly questionable,

as earlier evidence suggested separated flow over most of the flight regime. However, there are certain aspects that might be of interest. For example, it was shown by Jones *et al.*⁴ that the panel code predicted wake topologies accurately for nearly two-dimensional flows, even at very high reduced frequencies (see Fig. 1 for example). Unfortunately, with the very low aspect ratio of the MAV (≈ 4), the flows are likely to be very three-dimensional. Using the panel code to predict the performance of the MAV is further complicated by the aeroelastic deflection of the wings, making the angle of attack an unknown. (Aeroelastic modeling of these pitch deflections may be carried out in a future study.)

However, as no better numerical methods were available, the panel code was used to make a low-order estimate of the performance of the MAV. If the aeroelastic deflection of the wing is ignored, then the wings move with a plunge amplitude of $h = 0.3$ and $\Delta\alpha = 5$ degrees, with a phase angle of 180 degrees. In reality, as the frequency increases, the pitching approaches a phase angle of 270 degrees, as the wings feather under aerodynamic loading. In Figs. 19 and 20 the predicted thrust coefficient, C_t , and propulsive efficiency, η , are plotted as functions of the reduced frequency, k , and phase angle, ϕ . The predicted efficiencies may be quite high, above 90 percent, however, when the efficiency is high, the thrust coefficient is low, and if viscous losses are considered, the plot is likely to change drastically. Regions of both high efficiency and high thrust are of interest. The portion of the efficiency plot that drops below zero or is above 1 has been truncated for clarity. In this region the thrust is negative (drag, not thrust is generated), and over most of the area the power coefficient is also negative, indicating that the wing is fluttering (extracting energy from the flow). In these three-dimensional plots, the solid lines represent the value of the function indicated on the vertical axis, and the various dashed lines represent watermarks or isolevels of the function, as indicated in the legend in the upper right corner.

Figure 19 may be misleading due to the inverse relationship of the reduced frequency and the velocity. Dimensionalizing Fig. 19 to predict real thrust for a flapping frequency of 20Hz yields the results shown in Fig. 21. Note, the power has been limited according to the motor specifications and approximations for motor, gear and mechanical efficiencies. Of particular interest here is that as the velocity increases, the minimum thrust occurs for phase angles of 270 degrees (the angle for optimum efficiency), and the maximum occurs for phase angles between 90 and 180 degrees, however, the aerodynamic loading in that region is sufficient to saturate the motor.

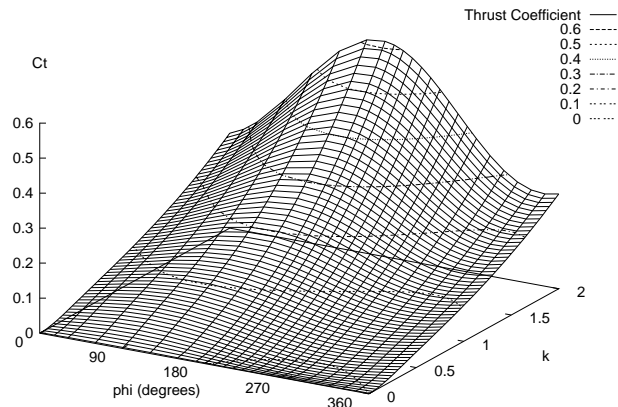


Fig. 19: Predicted thrust coefficient for the MAV.

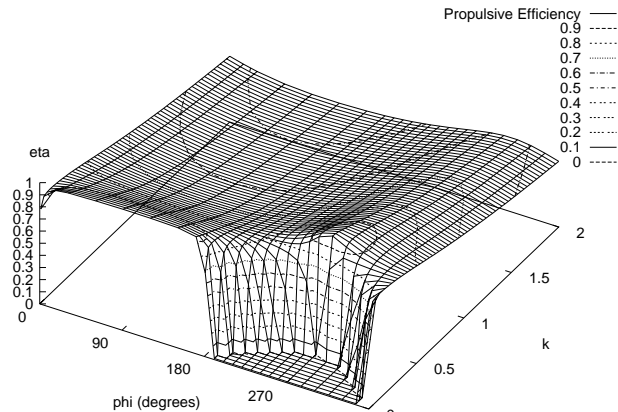


Fig. 20: Predicted efficiency for the MAV.

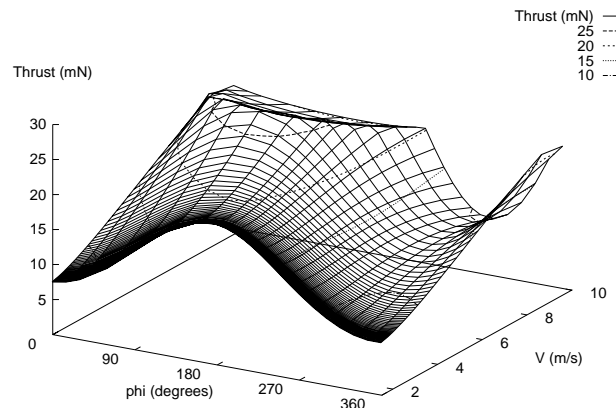


Fig. 21: Predicted thrust for the MAV at 20Hz.

Qualitative Flow Analysis

Using the smoke-wire, streaklines near the centerline are shown in Fig. 22 for a frequency of 10Hz and a velocity of 1.5m/s , resulting in a reduced frequency of about 1.5. The flow is remarkably planar, and the outline of a number of vortex structures can be seen. The wake topology predicted by the panel code for the same case is shown in Fig. 23, and is a pretty good representation of the real flow.

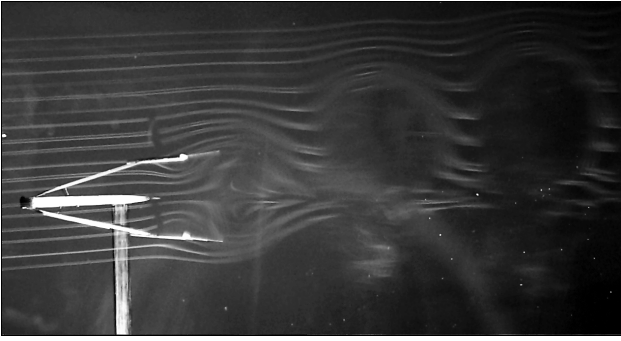


Fig. 22: Centerline wake topology at $k = 1.5$.

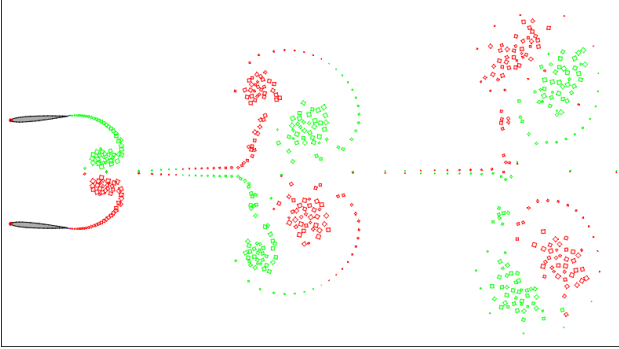


Fig. 23: Panel-code prediction of the wake.

Note, the wake shown for the panel code is indicated using a small square to represent a discrete vortex shed from each airfoil at each time-step to apply the Helmholtz condition. The size of each square indicates its vorticity magnitude, and the color indicates its orientation. Therefore, the panel code is essentially a *vorticity tagging* approach, and provides excellent detail of the evolution of the shed vorticity, but provides no visualization information on the external flow. The streaklines, on the other hand, provide an excellent view of the external flow, but virtually no information within the vortical structures.

Away from the centerline the flow becomes highly three-dimensional. At low reduced frequencies the tip vortices develop and evolve somewhat independently from one and other, that is, the vorticity on each changes sign as the wings plunge sinusoidally. However, at higher frequencies the nature of the flow changes considerably. In Figs. 24 and 25 streaklines released about half a chord length outside of the wing tips are shown from a rear-quarter view and a top view, respectively. The flow-speed is 1.5m/s , and the frequency is 20Hz , resulting in a reduced frequency of $k = 3.0$. The Strouhal number is difficult to estimate, due to the aeroelastic pitching of the wings, but it should be about 1.3.

The true nature of the flow is difficult to ascertain from Figs. 24 and 25. There appears to be massive flow entrainment from the sides, starting from about

the leading edge of the wing. The four tip vortices do not appear to sinusoidally change sign, although their strength must fluctuate. Looking from behind, the left, upper vortex rotates counter-clockwise, and its core turns toward the centerline, and is then deflected upward as it approaches the centerline. The other three trailing vortices are symmetric. A sketch of the primary trailing vortex structures is shown in Fig. 26.

In Jones and Platzer⁸ some effort was made to find easily constructed airfoil shapes that would yield high performance. While only static (wind-off) thrust generation was considered at the time, it was shown that a tear-drop shaped leading-edge spar with increased leading edge radius improved performance considerably over a thin, rectangular section leading edge. At that time, flow visualization was not performed, and while massive flow separation was suspected, it could not be confirmed.

Using the newly built smoke-wire, it was found that even at zero angle of attack, the flow would separate from both the upper and lower surfaces of the leading-edge spar, as shown in the sequence in Fig. 27.

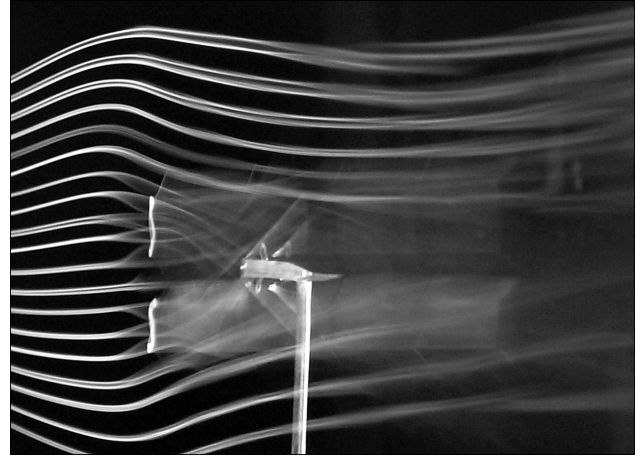


Fig. 24: Streaklines released $0.5c$ outside of wing-tip at $k = 3.0$.

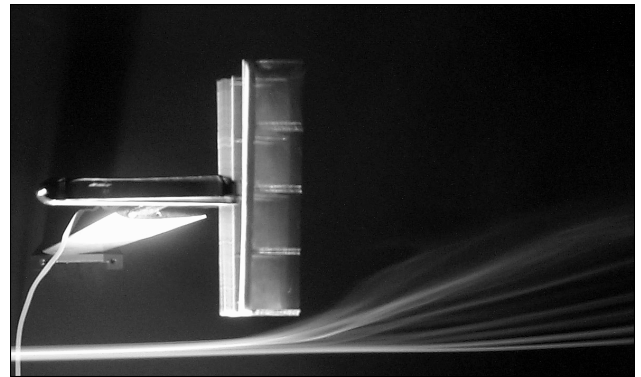


Fig. 25: Streaklines released $0.5c$ outside of wing-tip at $k = 3.0$.

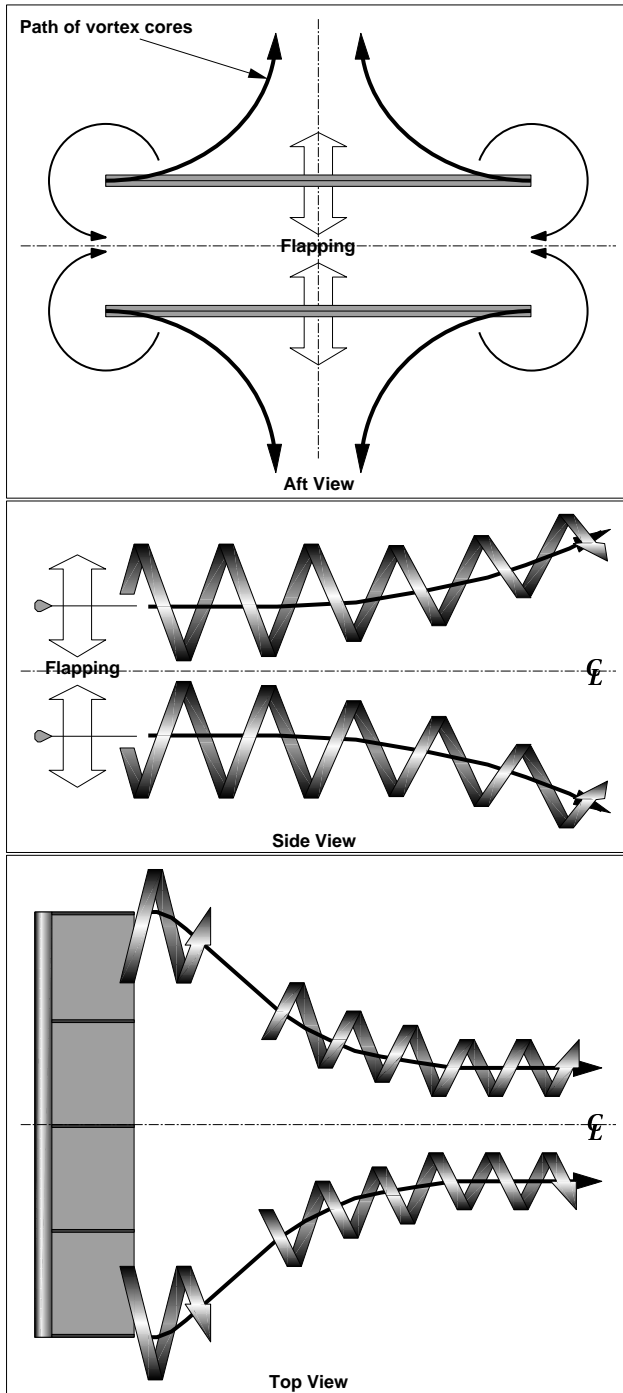


Fig. 26: Primary vortex structures at high frequency.

The tunnel speed was about 1.5m/s yielding a chord-Reynolds number of about 3,750. The photos were taken with a digital video camera, shooting 30f/s , and one full shedding cycle requires about 6 frames (the first and last frames are nearly identical), consequently, the shedding frequency should be approximately 5Hz. The tear-dropped leading-edge spar is clearly visible, but the rest of the airfoil is a bit harder to see. The leading-edge spar is about 6mm wide,

so the rest of the airfoil (essentially an infinitely thin splitter plate) extends about another 5-times the spar width downstream. Using the leading-edge thickness as the length-scale, the Strouhal number for this shedding is a very low 0.013, far below the natural shedding frequency of a cylinder. The surface roughness of the spars is quite high, due to the grain of the balsa wood, and the effect of this on shedding is unknown.

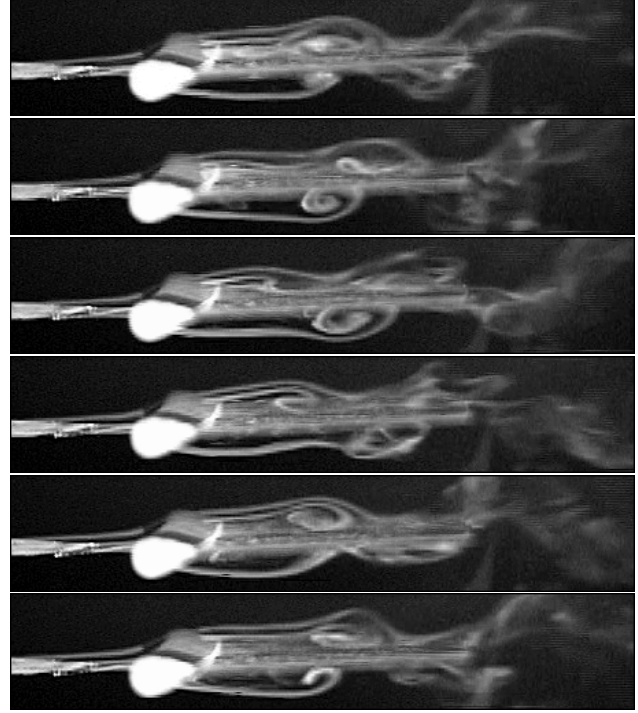


Fig. 27: Periodic shedding from the stationary leading edge.

Flapping the model at roughly 4Hz, resulting in a reduced frequency of roughly 0.6, the flow is completely separated on the suction-side of both wings, during both the outward and inward strokes, as shown in Fig. 28. The effective angle of attack in both cases is about 10 degrees.

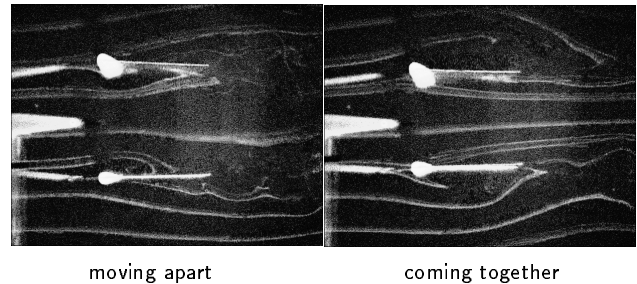


Fig. 28: Interior/exterior separation during flapping.

Quantitative Flow Analysis

In order to evaluate the thrust generation capabilities in the absence of the interference and drag

effects of the body and other components, the non-flapping profile drag is usually removed from the plotted thrust. In reality, the configuration drag is a function of the wing position, so the model is flapped at a very low frequency (typically about 0.1Hz), and the average drag is measured.

A typical, post-processed data-set is shown in Fig. 29 for the MAV with flexible wing mounts. The error bars indicate the estimated error in the measurements. Theory predicts that the thrust should increase as the frequency squared, and while this is confirmed for low and moderate frequencies, for the static and low-speed cases the thrust curves have a notable kink at high frequency. This is due to a mechanical limitation of the aeroelastic wing deflections. In the static case, at about 20Hz the wing trailing edges actually meet in the middle, as shown in Fig. 15, and further deflections are not possible, apparently leading to losses at higher frequencies.

To save time during data acquisition, an imprecise selection of velocities and frequencies are used, and then the data is mapped to a rectangular grid using spline interpolation allowing for more direct comparisons between the various configurations. The resulting interpolated data from Fig. 29 is shown in Fig. 30 as a surface plot of thrust as a function of frequency and velocity, with isolevels as indicated in the legend.

As with the previous study, the maximum thrust is still found at zero velocity, but with the increased frequency available due to the closed-loop controller, the model now generates about $75mN$ of thrust; enough to make the unballasted model hover! The MAV's profile drag at $9.5m/s$ tunnel speed is just $70mN$. Unfortunately, as the speed is increased the thrust is reduced. In Fig. 31 the net thrust (profile drag included) is plotted, and it can be seen that the MAV does not overcome drag beyond $5.5m/s$.

Next the stiffness of the wing-mounts was varied. This was a pretty difficult parameter to quantify, as the material properties of the carbon-fiber strips was not constant. Three values were considered; the flexible version shown above, a semi-rigid mount, where the length of the carbon-fiber strips was halved, and a rigid version where a balsa support was glued on to keep the wing geometry fixed. In reality, the wings were still quite elastic as the carbon-fiber ribs allowed the camber to change. The results for the three cases are shown in Fig. 32, with the three line-types indicating the different configurations, as indicated in the legend. The three surfaces cover the full velocity range but cover varying frequency ranges, determined by the available power.

The flexible wing model performs better at all flow speeds and frequencies under about 20Hz, but at

higher frequencies the semi-rigid and rigid-mount variations overtake the flexible-wing model. Unfortunately the aerodynamic load also increases for the semi-rigid and rigid-wing models, preventing them from reaching the higher frequencies, as the motor runs out of torque.

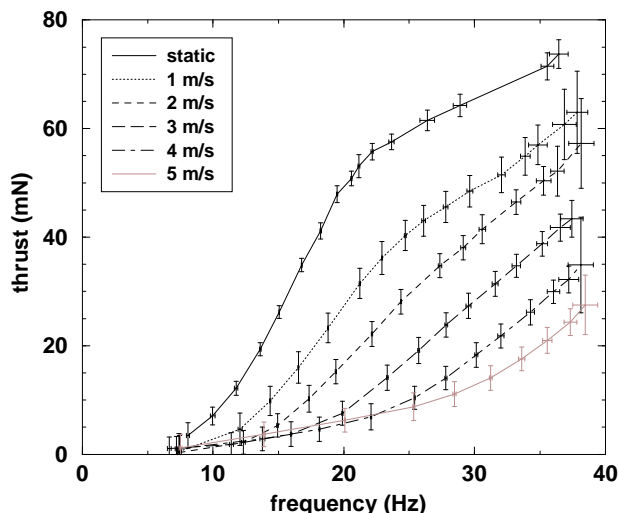


Fig. 29: Typical thrust data for the MAV.

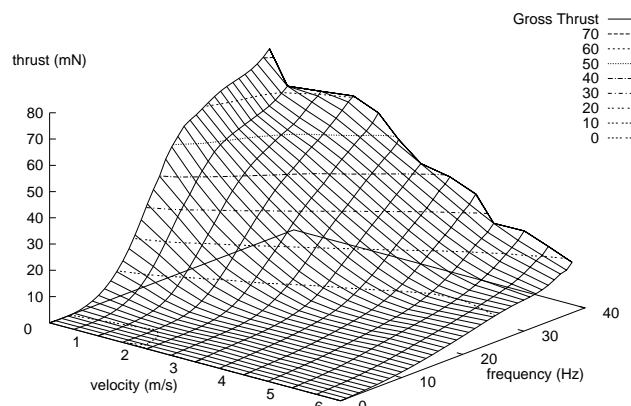


Fig. 30: Thrust for the flexible-wing MAV.

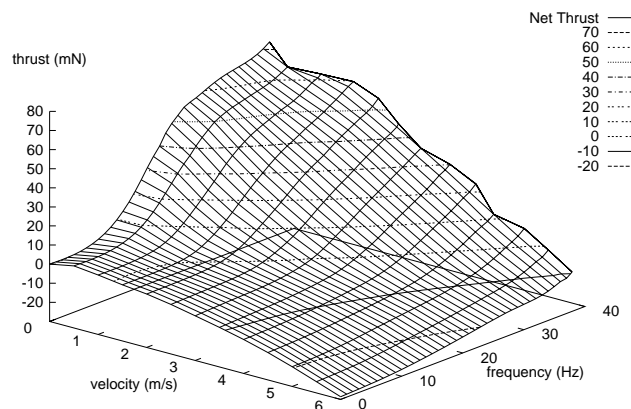


Fig. 31: Net thrust for the flexible-wing MAV.

Tip plates were added to the model in an attempt to reduce tip-losses. The tip-plates were rather minimal, structurally, and consequently they tended to flex quite a bit during operation. The effect of this deformation is not known, but the end result is that, if anything, the tip plates reduced the thrust, both for the flexible wing-mount model and, to a lesser degree, for the rigid wing-mount model, as shown in Figs. 33 and 34, respectively.

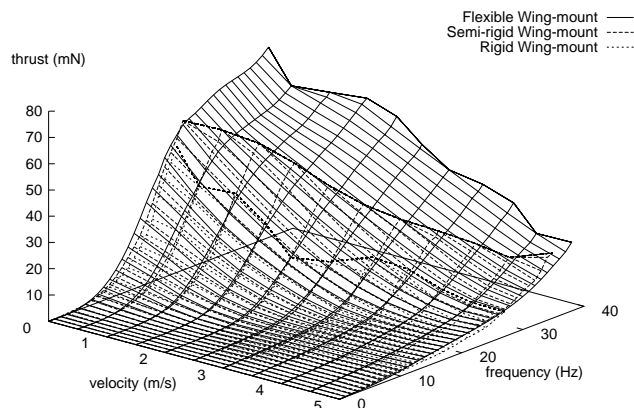


Fig. 32: Thrust versus wing-mount stiffness.

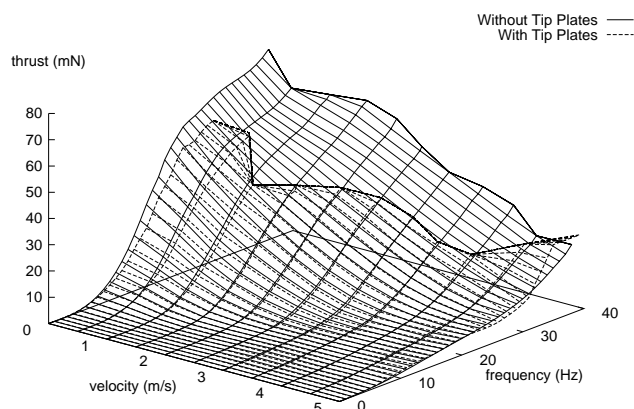


Fig. 33: Effect of tip-plates for the flexible wing model.

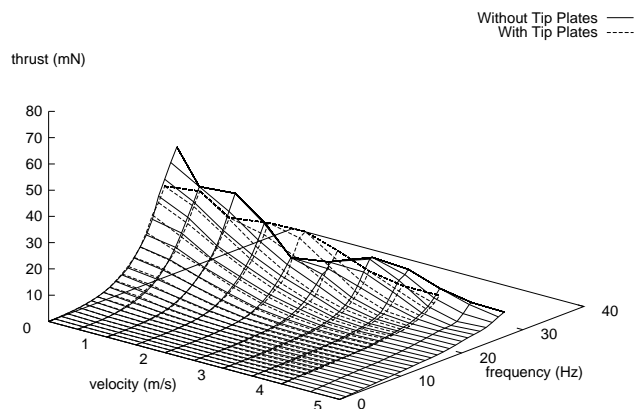


Fig. 34: Effect of tip-plates for the rigid wing model.

The maximum frequencies attained with the tip-plates mounted were generally lower than without the tip-plates, however, this was often not due to power saturation, but rather to model vibrations that either prevented accurate thrust measurements or broke support wires. The tip-plates will be replaced with a more structurally sound design in the future. Additionally, flow-visualization with the tip-plates added will be performed to gauge their influence on the overall flow.

Conclusions

An effort was made to refine and improve the design, manufacture and testing of flapping-wing micro air vehicles. The newer model increased the model modularity and reliability, adding a heat-sink to enable higher motor loads without damaging the motor, replacing the Japanese tissue wing skin with micro-film for lighter weight and improved visualization, and replacing the open-loop controller with a closed-loop version which could drive the model at over 38Hz. Additionally, improvements in the testing of the models were made both quantitatively, for the direct measurement of thrust, and qualitatively, for the visualization of these highly three-dimensional, separated flows.

A smoke-wire was built to provide uniformly spaced streaklines at low flow speeds, and visualization helped to characterize the flow. While earlier tests demonstrated the thrust improvements of the current airfoil design, visualization proved that even at zero angle of attack, vortex shedding was present on both sides of the leading-edge spar. At reduced frequencies as low as 0.6 the flow was completely separated from the suction side of the airfoil throughout the flapping cycle. Visualization demonstrated that flow at the centerline remained planar, even at high frequencies, with a wake topology that was accurately modeled by a panel code. However, the flow away from the centerline was found to be highly three-dimensional, and changed significantly with frequency.

Direct thrust measurements produced similar trends to past studies, producing the highest thrust at zero flight speed. However, with the much higher frequency afforded by the closed-loop controller, the new model produced 7 times the thrust of the previous study. The new model produced enough thrust to hover, and overcame its own drag up to 5.5 meters per second. The model employed aeroelastic feathering of the wings. It was shown that while the thrust at a specific velocity and frequency was relatively insensitive to the stiffness of the aeroelastic joint, the motor load was reduced with more flexible wing mounts, allowing the model to reach much higher frequencies, ultimately

leading to higher thrust. The effect of tip-plates was also investigated, and while the current results suggest that they do not improve performance, further testing is needed to confirm this.

Several additional model design variations are currently under investigation, including models with variable plunge amplitude and mean separation. Additional variations include articulated pitching so that the model maintains a fixed angle of attack, and a wing with passive camber control. Flow visualization will be used to further explore these complicated flow-fields, aiding in the design optimization. The smoke wire is limited to the velocity range of 1 to 3 meters per second. A conventional fog machine together with a laser light sheet will be used to explore the flow outside this range. Additionally, encoded LDV will be used to probe the localized flow enabling an improved understanding of the unsteady flow, and comparisons may be made with unsteady Navier-Stokes solutions that are currently underway.

Acknowledgments

This investigation was supported by the Naval Research Laboratory under project monitors Kevin Ailinger and Jill Dahlburg and by the Naval Postgraduate School direct research program.

References

- ¹ Knoller, R., "Die Gesetze des Luftwiderstandes," **Flug- und Motortechnik (Wien)**, Vol. 3, No. 21, 1909, pp. 1-7.
- ² Betz, A., "Ein Beitrag zur Erklärung des Segelfluges," **Zeitschrift für Flugtechnik und Motorluftschiffahrt**, Vol. 3, Jan. 1912, pp. 269-272.
- ³ Jones, K. D., Lund, T. C. and Platzter, M. F., "Experimental and Computational Investigation of Flapping-Wing Propulsion for Micro-Air Vehicles," presented at the *Conference on Fixed, Flapping and Rotary Wing Vehicles at Very Low Reynolds Numbers*, Notre Dame, Indiana, June 5-7, 2000.
- ⁴ Jones, K. D., Dohring, C. M. and Platzter, M. F., "Experimental and Computational Investigation of the Knoller-Betz Effect," **AIAA Journal**, Vol. 36, No. 7, May 1998.
- ⁵ Jones, K. D. and Platzter, M. F., "Numerical Computation of Flapping-Wing Propulsion and Power Extraction," AIAA Paper No. 97-0826, Jan. 1997.
- ⁶ Garrick, I. E., "Propulsion of a Flapping and Oscillating Airfoil," NACA Report 567, 1936.
- ⁷ Jones, K. D. and Platzter, M. F., "An Experimental and Numerical Investigation of Flapping-Wing Propulsion," AIAA Paper No. 99-0995, Jan. 1999.
- ⁸ Jones, K. D. and Platzter, M. F., "Flapping-Wing Propulsion for a Micro Air Vehicle," AIAA Paper No. 2000-0897, Jan. 2000.
- ⁹ Schmidt, W., "Der Wellpropeller, ein neuer Antrieb fuer Wasser-, Land-, und Luftfahrzeuge," **Z. Flugwiss.** Vol. 13, 1965, pp. 472-479.
- ¹⁰ Lund, T. C., "A Computational and Experimental Investigation of Flapping Wing Propulsion," Master's Thesis, Dept. of Aeronautics and Astronautics, Naval Postgraduate School, Monterey, CA, March 2000.
- ¹¹ Duggan, S. J., "An Experimental Investigation of Flapping Wing Propulsion for Micro Air Vehicles," Master's Thesis, Dept. of Aeronautics and Astronautics, Naval Postgraduate School, Monterey, CA, June 2000.
- ¹² Teng, N. H., "The Development of a Computer Code for the Numerical Solution of Unsteady, Inviscid and Incompressible Flow over an Airfoil," Master's Thesis, Naval Postgraduate School, Monterey, CA, June 1987.
- ¹³ Pang, C. K., "A Computer Code for Unsteady Incompressible Flow past Two Airfoils," Aeronautical Engineer's Thesis, Dept. of Aeronautics and Astronautics, Naval Postgraduate School, Monterey, CA, Sept. 1988.
- ¹⁴ Hess, J. L. and Smith, A. M. O., "Calculation of Potential Flow about Arbitrary Bodies," **Progress in Aeronautical Sciences**, Vol. 8, pp. 1-138, Pergamon Press, Oxford, 1966.
- ¹⁵ Basu, B. C. and Hancock, G. J., "The Unsteady Motion of a Two-Dimensional Aerofoil in Incompressible Inviscid Flow," **Journal of Fluid Mechanics**, Vol. 87, 1978, pp. 159-168.
- ¹⁶ Pope, A., Wind-Tunnel Testing, Second Edition, John Wiley & Sons, Inc., New York, 1954.